"Application of Remote Sensing Methods for Mapping Hydrothermal Minerals and Alterations Zones in the Qahestan Mountain Range, Southwest of Qaen County, Northeastern Iran."

Arman Shahmoradi [a*] ,Mohammad Yazdi [a]

[a] University of Shahid Beheshti, Faculty of Earth Science, Department of Geology, Tehran, Iran
* Corresponding author's E-mail address: armanshahmoraadi@gmail.com

Abstract

Utilizing remote sensing data has become integral in modern exploration processes, offering an economically efficient method for comprehensive mineral exploration. This study focuses on the application of ASTER (Advanced Spaceborne Thermal Emission and Reflection Radiometer) remote sensing data, particularly in the Visible-Near Infrared (VNIR) and Short Wave Infrared (SWIR) ranges, for mapping hydrothermal minerals and alterations in the Qaen County of South Khorasan Province, northeastern Iran. The study area, characterized by sparse vegetation and significant mineral potential, allows for practical remote sensing analysis. The geological complexity of the region, including lithological variations from Proterozoic to Mesozoic units, active tectonics, and diverse alteration zones, necessitates a multi-method approach for accurate mapping. The analytical methods employed include False Color Composite (FCC), Band Ratio (BR), Relative Band Depth (RBD), and Matched Filtering (MF). These methods highlight alterations associated with minerals such as kaolinite, muscovite, epidote, and malachite.

Results demonstrate the efficacy of these methods in providing a detailed overview of the study area. The FCC method offers a broad perspective, while the BR and MF methods excel in accuracy and detail. The region's low vegetation cover enhances the precision of the analysis, further supported by the removal of vegetation using the Normalized Difference Vegetation Index (NDVI) method. Specific alterations, such as argillic, phyllic, and propylitic, are successfully identified and correlated with the geological units in the area. The presence of kaolinite and argillic alteration in the central region and the co-occurrence of muscovite and malachite indicates potential mineralization. The study suggests the existence of porphyry copper and epithermal mineralization systems in the study area. In conclusion, integrating ASTER remote sensing data with diverse analytical methods is a powerful tool for mapping hydrothermal minerals and alterations in geologically complex regions, contributing valuable insights for mineral exploration and resource assessment.

.

Keywords: Qaen, ASTER, Alteration mapping, Copper, Iran, MF

1. Introduction

Utilizing remote sensing data constitutes a critical and consequential facet of the exploration process (Ahmadirouahni et al., 2018; Moradpour et al., 2021). Remote sensing data, introduced in the 1940s, has demonstrated its effectiveness as an economically efficient exploration method. Its capacity to provide a comprehensive and in-depth perspective and its multispectral capabilities contribute to cost reduction. Notably, among the spectrum of sensors, the ASTER sensor emerges as a critical instrument in the differentiation and identification of minerals, alterations, and tectonic features (Crosta et al., 2003; Tangestani et al., 2008; Hewson & Cudahy, 2011; Moghtaderi et al., 2017). The ASTER sensor has three bands in the Visible-Near Infrared (VNIR) range, spanning from 0.52 to 0.86 µm and featuring a spatial resolution of 15 meters. Additionally, it incorporates six bands in the Short Wave Infrared (SWIR) spectrum, covering 1.6 to 2.5 µm, with a spatial resolution of 30 meters. Furthermore, the Thermal Infrared (TIR) bands exhibit a significantly lower spatial resolution, approximately 90 meters, and consist of five bands within the 8.1 to 11 µm range (Table 1). In this study, emphasis is placed on utilizing the SWIR and VNIR spectra (Fujisada,1995; Abram, 2000; Rowan & Mars, 2003; Rowan et al., 2005; Abram, 2015) solely. The study area is situated within the Qaen County of South Khorasan Province, located in northeastern Iran, specifically in the Qahestan mountain range. Within this region, the investigation is focused on surface anomalies and geochemical characteristics associated with elements including Fe, Cu, Pb, Zn, and Ni. The area encompasses notable elevations such as Mount Zul, reaching an elevation of 2361 meters; Mount Sargol, surrounded by mountains with elevations of 2150 meters; Mount Lakhha-ye-tangle at 2012 meters; and Mount Abidar at 2210 meters (Fig 1). These geological features contribute to a more concentrated and purposeful deployment of remote sensing activities and operations (Berthiaux et al., 1979; Alipour et al., 2008).

Table 1 Characteristics of the 3 ASTER Sensor Systems (Fujisada, 1995; Abram 2000).

Subsystem	Band No.	Spectral Range (µm)	Spatial Resolution (m)	Quantization Levels
VNIR	1	0.52 – 0.60	15	8 bits
	2	0.63 – 0.69		
	3N	0.78 – 0.86		
	3B	0.78 – 0.86		
SWIR	4	1.60 – 1.70	30	8 bits
	5	2.145 – 2.185		
	6	2.185 – 2.225		
	7	2.235 – 2.285		
	8	2.295 – 2.365		
	9	2.360 – 2.430		
TIR	10	8.125 – 8.475	90	12 bits
	11	8.475 – 8.825		
	12	8.925 – 9.275		
	13	10.25 – 10.95		
	14	10.95 – 11.65		

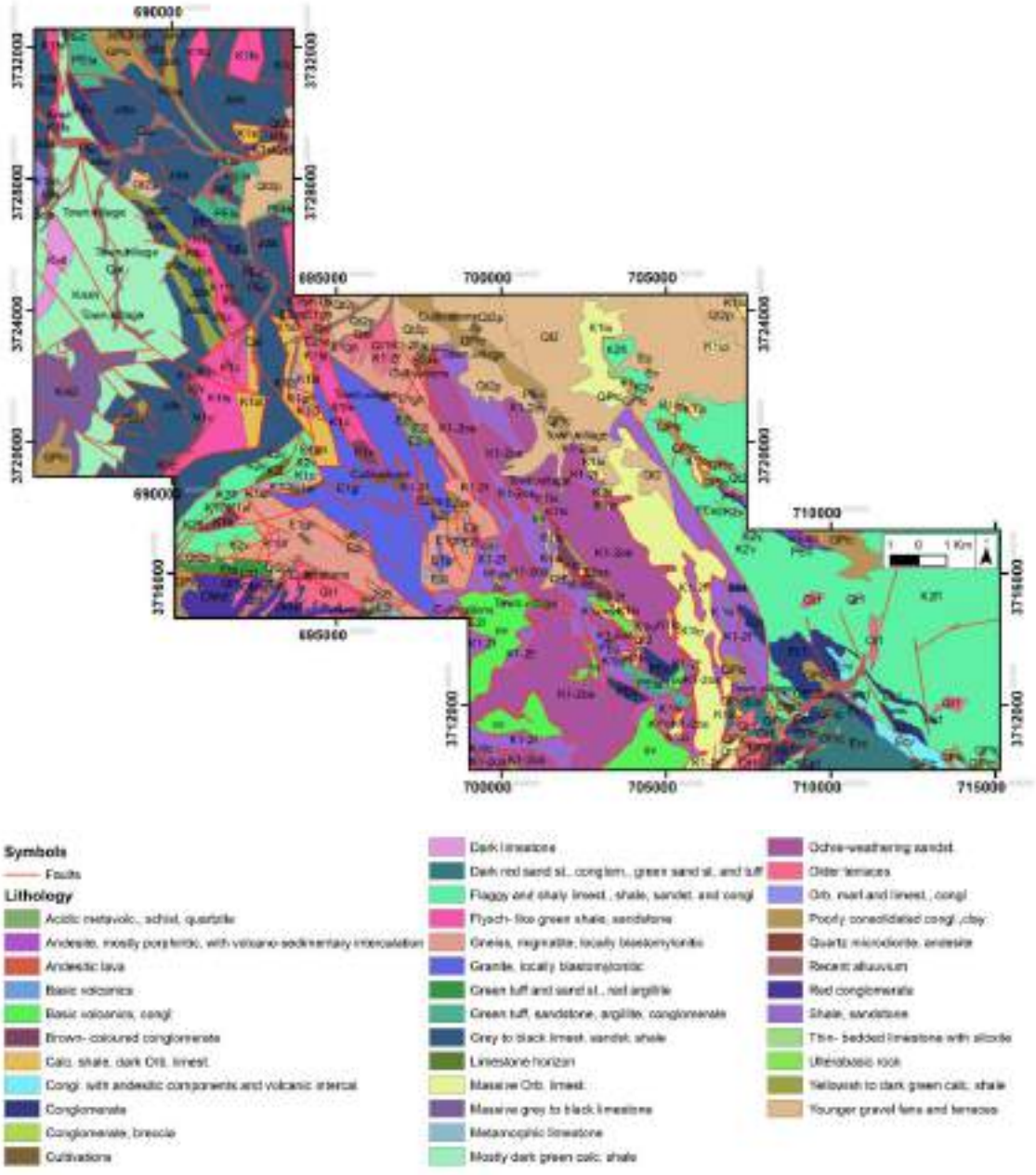

Fig 1 Geology map of the study area (Berthiaux et al., 1979).

2. Geological Setting

The studied area encompasses approximately 354 Km^2, with coordinates ranging from north 33°50 to 33°71 and east 59° to 59°32, situated within the flysch Zone in eastern Iran (Stöcklin et al., 1972; Aghanabati., 2004). According to studies (Camp & Griffis., 1982; Tirrul et al., 1983), this Flysch zone is a volcanic zone located between the Lut Block and Afghanistan. The eastern Iranian Flysch Basin is covered by oceanic pelagic sediment overlain by younger deposits influenced by recent magmatism.

According to (Gorbani et al., 2000; Maghsoudi 2005; Gorbani., 2013), this region is part of a zone containing ophiolitic assemblages associated with manganese originating from magmatic sources. Additionally, within the Ultramafic Complex are magmatic rocks and flysch units in the mineralization zone of Au, Pb, Zn, and Cu with a skarn-hydrothermal origin.

Lithological units of Mesozoic age dominate, covering a more significant extent of the region. Nevertheless, the oldest lithological units revert to the Proterozoic era, particularly in the central part of the area within the Zul and Abidar mountains. In this section, the rocks, frequently trending in the NW-SE direction, consist predominantly of gneiss, granite, and metamorphosed sediments (Berthiaux et al., 1979; Aghanabati., 1998; Berthiaux et al., 1999). Mesozoic units are more pronounced, particularly in the western and northwestern parts of the region surrounding the Gazik area. In these areas, Jurassic and Lower Cretaceous units of the Neocomin age are prevalent, encompassing dark limestone from the Qaleh Dokhtar Formation. Sandstones and yellow shales accompany these units. Upper Cretaceous units contain the eastern and southeastern portions of the region, constituting a flysch-like sequence characterized by green shales and sandstones interleaved with volcanic layers. In the southeastern part, volcanic-ophiolitic units are covered by the flysch unit. Paleocene units are primarily covered by Eocene units, where the Eocene unit, forming the Lakhdizuk Formation around the Lakhha-ye-Tangal mountain, is juxtaposed with the Upper Cretaceous unit. Quaternary units extend northwards towards Qaen (Berthiaux et al., 1979). The region is tectonically active, and dominant fault zones and fractures are concentrated in the central part of the area (Fig 2). The types of faults in the region can be classified into strike-slip and thrust faults. The trend of faults and fractures, as depicted in the rose diagram (Fig 3), aligns with the NW-SE direction, similar to the trend of the rocks in the region (Fig 4) (Berthiaux et al., 1979; Berberian et al., 1981).

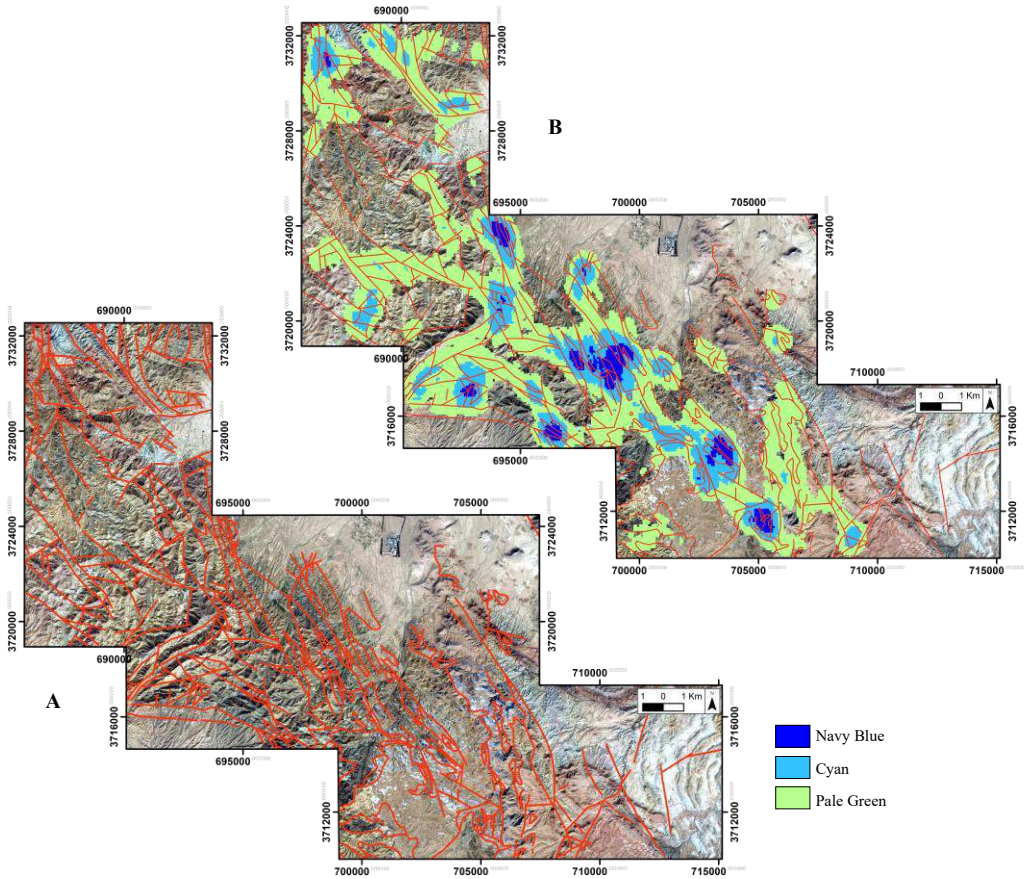

Fig 2 A) The map of faults and fractures (Berthiaux et al., 1979). B) Density map of faults and fractures, To rank the colors by density from highest to lowest: 1) Navy Blue 2) Cyan 3) Pale Green.

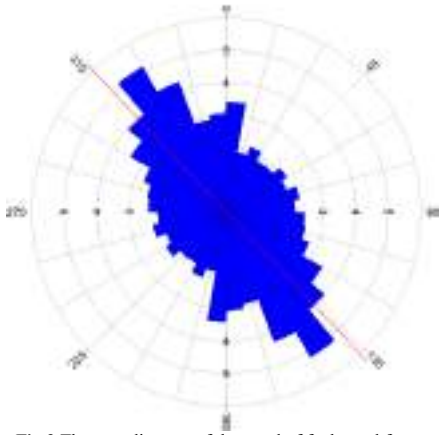

Fig 3 The rose diagram of the trend of faults and fractures.

Fig 4 Images of faults within the region serving as boundaries between geological units .A) Mount Asheghan, north of the area; B) Mount Lakhha-ye-Tangal, South of the area.

3. Materials and methods

The selection of this region was based on the limited availability of strong and reliable remote sensing data until now. On the one hand, the area is characterized by a sparse vegetation cover, an arid and desert-like climate, and significant mineral potential in the surrounding areas. These conditions create an opportunity for utilization and examination using (ASTER) data to highlight and map Mineral alteration. Therefore, ASTER data with the following identification number AST_L1T_00306172007065520_20150519230008_119061 have been utilized in this article.

Identifying altered minerals is based on spectral features and absorption and reflection bands. Therefore, in the alteration of average argillic minerals(Fig 5), whose indicative minerals such as kaolinite, alunite, and montmorillonite have Al-O-H bonding, kaolinite exhibits strong absorption in the spectral range of 2200 nanometers (SWIR band 6) and secondary absorption at 2170 nanometers (SWIR band 5) (Hunt., 1977; Hunt & Ashley., 1979; Mars & Rowan., 2004; Mars., 2014; Liu et al., 2018).

The alteration zone of phyllic or sericitic is characterized by minerals such as muscovite, illite, and, to some extent, quartz. Muscovite and illite, with Al-O-H bonding similar to indicative minerals in argillic alteration, exhibit absorption in the spectral range of 2200 nanometers (SWIR band 6) and weaker absorption in the range of 2330 to 2380 nanometers (SWIR band 8) (Hunt., 1977; Hunt & Ashley., 1979; Mars & Rowan., 2004; Mars., 2014; Liu et al., 2018). In the propylitic alteration zone, indicative minerals include chlorite, epidote, and calcite, characterized by Fe-Mg-O-H bonding. They exhibit strong absorption in the spectral range of 2320 to 2335 nanometers (SWIR band 8) and secondary weak absorption at 2250 nanometers (near SWIR band 7) (Hunt., 1977; Hunt & Ashley., 1979; Mars & Rowan., 2004; Mars., 2014; Liu et al., 2018). After preparing the initial data, the workflow continues in three stages: pre-processing, processing, and post-processing using the software ENVI 5.6, ArcMap 10.8, and ERDAS IMAGINE 16.7(Amer., 2010; Hewson & Cudahy., 2005; Hewson & Cudahy., 2011).

3.1. Pre-processing

To utilize ASTER data, it is essential to conduct pre-processing procedures. The used image is georeferenced with the UTM coordinate system, Zone 40 (WGS1984), as the reference datum.

Initially, each VNIR and SWIR spectra underwent separate geometric and radiometric corrections, with atmospheric corrections applied using the IARR and FLAASH algorithms for precision (Kruse.,1988; Ben-Dor & Kruse., 1994; Matthew et al., 2002; QUAC., 2009; Liang & Wang., 2012; Modabberi et al., 2107). Subsequently, these two spectra were stacked; however, it is noteworthy that the pixel size was set to 30 meters due to the lower resolving power of SWIR compared to VNIR, which could lead to complications in the subsequent stages. Following these steps and corrections, the Pan Sharpening Gram Schmit algorithm enhanced the image's spectral and spatial capabilities. At the end of the preprocessing

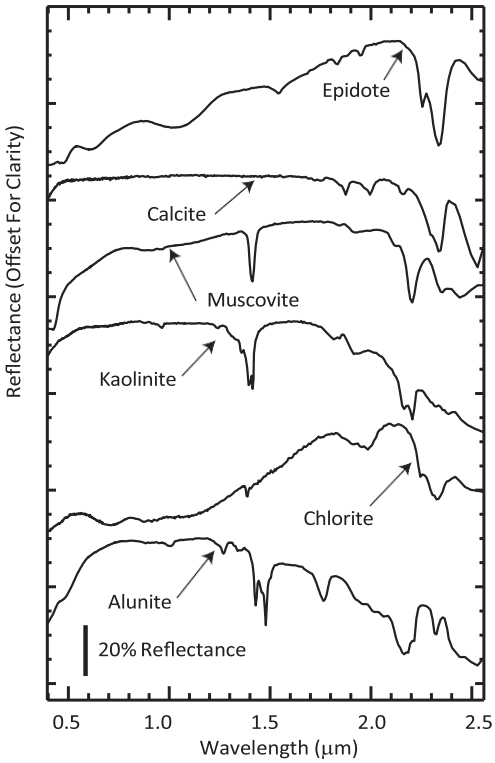

Fig 5 Laboratory spectra of epidote, calcite, muscovite, kaolinite, chlorite, and alunite, which a common hydrothermal alteration minerals (Clark et al., 1993).

stages, the vegetative cover must be removed from the image to prevent interference with alterations such as argillic. For this purpose, the NDVI algorithm with R = 2 and NIR = 3 was applied to identify these areas, and a mask was created. As a result, the subsequent processing steps will not be affected (Iwasaki et al., 2002; Hewson & Cudahy., 2005; Amer., 2010; Testa et al., 2018).

3.2. Processing

1. False Color Composite (FCC)

Based on the combination of multiple spectral bands, the false color composite method proves highly beneficial in identifying alteration zones, the lithology of the region, and more (Moghtaderi et al., 2007; Jun et al., 2008; Alimohammadi et al., 2015; Liu et al., 2018). This study employed a combination of the 468 and 531 color bands. The 468 color combination (RGB) is a commonly used technique for detecting argillic alteration zones (kaolinite), phyllic alteration zones (sericite and muscovite), and propylitic alteration zones (calcite and epidote) (Boloki & Poormirzaee., 2010; Azizi et al., 2010; Alimohammadi et al., 2015; Liu et al., 2018; Shahmoradi & Yazdi., 2023).

The 631 color combination (RGB) is utilized for distinguishing geological units, and by correlating with the geological map of the region, it becomes possible to identify the lithological type associated with each color (Adiri et al., 2016; Marzouki & Dridri., 2023; Shahmoradi & Yazdi., 2023).

2. Band Ratio

The band ratio method is one of the standard techniques in satellite image processing, widely utilized in geology for detecting lithology, mineralogy, and alterations (Rowan et al., 1977; Mars & Rowan., 2006; Zhang et al., 2007; Liu et al., 2018; Boloki & Poormirzaee., 2010; Moradpour et al., 2021; Tahir & Caner., 2022). This method involves dividing two bands by each other, where the band with high reflectance from the target is placed in the numerator, and the band with high absorption is placed in the denominator. The band ratio method is a foundational approach in image processing, with techniques such as RBD and logical algorithms like IDL (Mars & Rowan., 2006) performing analyses based on this method. In this study, the RBD method has also been employed. It is worth noting that this method has also been applied in the preprocessing stage, where dividing band 3 by band 2 allows for identifying vegetation covers in the image (Mars & Rowan., 2006).

3. Relative Band Depth (RBD)

The Relative Band Depth method was introduced by Crowley et al., 1989, and is one of the efficient techniques in image processing and enhancement. This method places the band closest to the minimum absorption position in the denominator to enhance the target. In the numerator, the fraction consists of the sum of two bands that represent adjacent reflectance. This research identifies the foundations of Fe-Mg-O-H, Al-O-H, and CO_3^{2-} (Rowan et al., 2006; Liu et al., 2018).

4. Matched Filtering (MF)

The Matched Filtering method is another image processing technique in which the responses of purely known mineral spectra, also known as endmembers, are enhanced, and background responses are minimized. This method is utilized for mineral identification based on matching the endmember spectra with the image spectra (Harsanyi et al., 1994; Bedini., 2011; Liu et al., 2018). The algorithm determines the abundance of each predefined element in the image by employing spectral unmixing (Boardman et al., 1995). In this research, the spectral library from the USGS is the basis for the spectra.

3.3. Post-processing

1. False Color Composite (FCC) Result

Initially, Fig 6, resulting from the false color composite (RGB=468), is presented, indicating argillic, phyllic, and propylitic alteration zones, each highlighted in a distinctive color spectrum. Moderate to advanced argillic alteration appears in shades from pink to red, predominantly covering the central part around the Zul village and the western part of the area.

Phyllic alteration zones, similar to argillic zones, have an Al-O-H basis, with altered muscovite alongside kaolinite. These two zones overlap, with the phyllic alteration zone, particularly in the western region around Chedan-e-bala village and Sargol Mountain, appearing in the dark to light pink.

Propylitic alteration, characterized by CO_3^{2-} foundation and calcite, is observed around carbonate rocks in the region's eastern part, notably in the Lakhha-ye-tangal mountain area, depicted in yellow to green in the image. Fig 7a, illustrates the RGB=631 color combination, where various lithological units are distinguished by different colors, aiding in initial exploratory studies. Fig 7b, combines the geological units (Berthiaux et al., 1979) with the false-color composite image RGB=631, demonstrating the correspondence of each color to a specific geological unit.

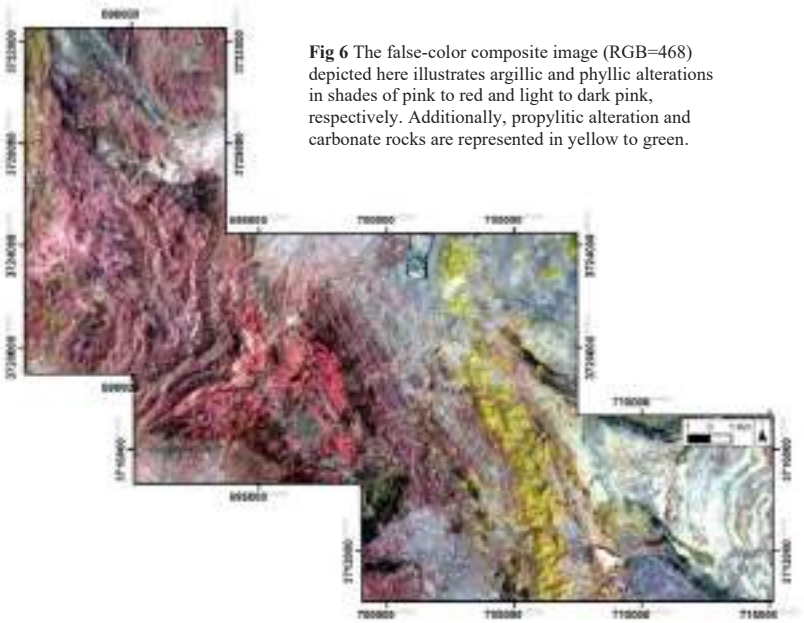

Fig 6 The false-color composite image (RGB=468) depicted here illustrates argillic and phyllic alterations in shades of pink to red and light to dark pink, respectively. Additionally, propylitic alteration and carbonate rocks are represented in yellow to green.

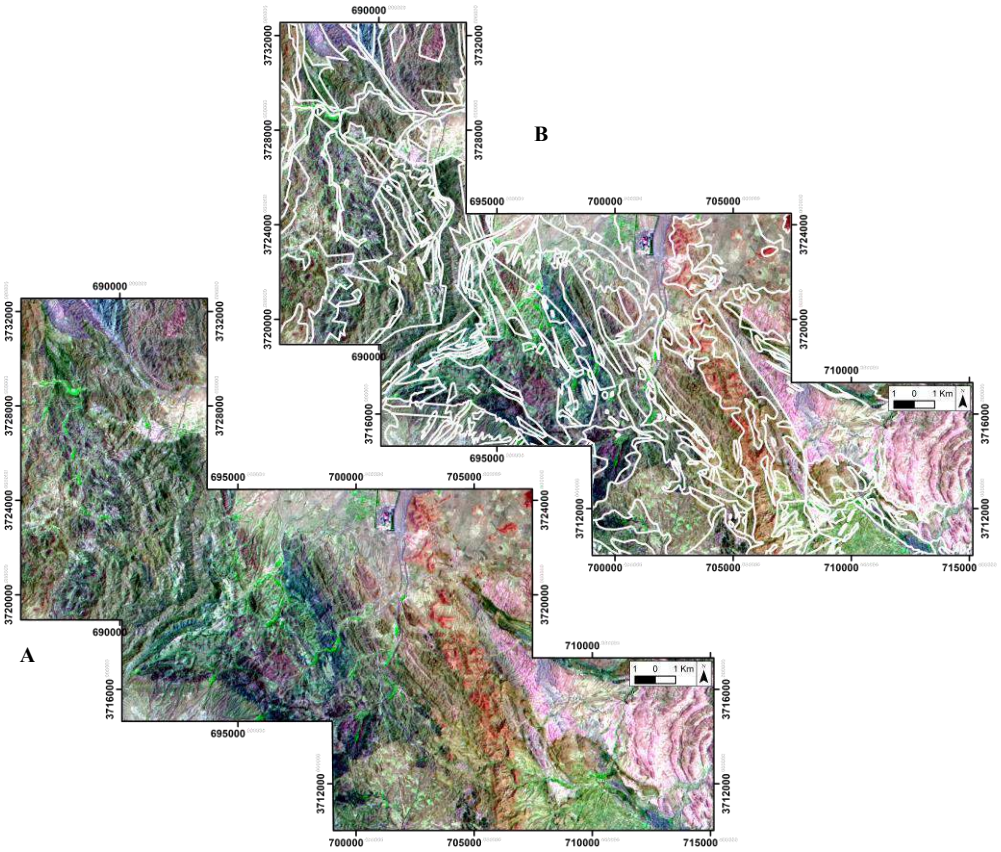

Fig 7 A)The false-color composite image (RGB=631) indicates lithological units. B) False color composite image combined with the boundary of geological units.

2. Band Ratio Result

The selection of specific bands for band ratios is determined by considering the shape of the reflectance spectrum for each mineral. Bands encompassing the targeted mineral or rock's maximum and minimum reflectance values are chosen. In the resulting image, bright points or pixels represent the target areas. Since the images are single-band and black and white, assigning band ratios to red, green, and blue (RGB) colors form a false-color composite image for better examination.

Specific minerals indicative of these alterations detect propylitic, phyllic, and argillic alterations. In argillic alteration, the band with the highest absorption is in band 6, and the band with the highest reflectance is in band 4. Therefore, a band ratio of 4 to 6 (4/6) can be helpful for identification. Similarly, in phyllic alteration, the band with the highest absorption is band 6, and the band with the highest reflectance is band 5, so the band ratio of 5 to 6 (5/6) is indicative. For propylitic alteration, bands 8 and 5 have the highest absorption and reflectance, respectively. A band ratio of 5 to 8 (5/8) is employed for enhancement. Fig 8, a false-color composite (R=4/6, G=5/8, B=5/6), reveals propylitic alteration zones in green in the eastern part of the area. The dominant pink color corresponds to argillic alteration, and the blue color corresponds to phyllic alteration. Notably, these two alterations overlap, and areas with shades of purple have varying contributions from both alteration types.

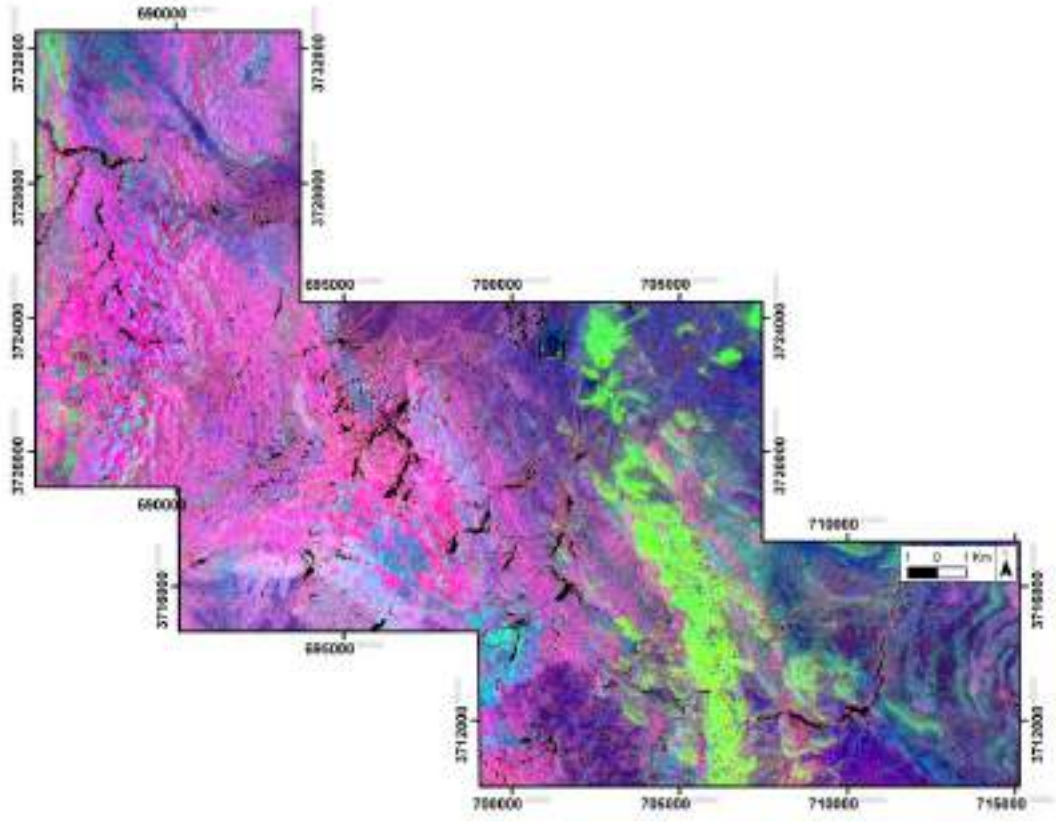

Fig 8 A false-color composite R=4/6, G=5/8, B=5/6. Which represents each of the alteration zones mentioned in the text.

3. Relative Band Depth (RBD) Result

This method has been utilized to highlight altered zones based on the specified band ratios. Specifically, RBD5 (Equation 1) (Fig 9a) has been employed to accentuate kaolinite and argillic alteration, RBD6 (Equation 2) (Fig 9b) for muscovite and phyllic alteration zones, and RBD8 (Equation 3) (Fig 9c) for propylitic alteration zones. Finally, a false-color composite image (Fig 9) was created for a comprehensive view and better understanding using the formula (R=RBD8, G=RBD6, B=RBD5). In this image (Fig 9d), the pink color represents propylitic alteration zones, green indicates phyllic alteration zones, and blue signifies argillic alteration zones.

Equation 1 RBD5 = (Band4 + Band6) / (2× Band5)
Equation 2 RBD6 = (Band5 + Band7) / (2× Band6)
Equation 3 RBD8 = (Band7 + Band9) / (2× Band8)

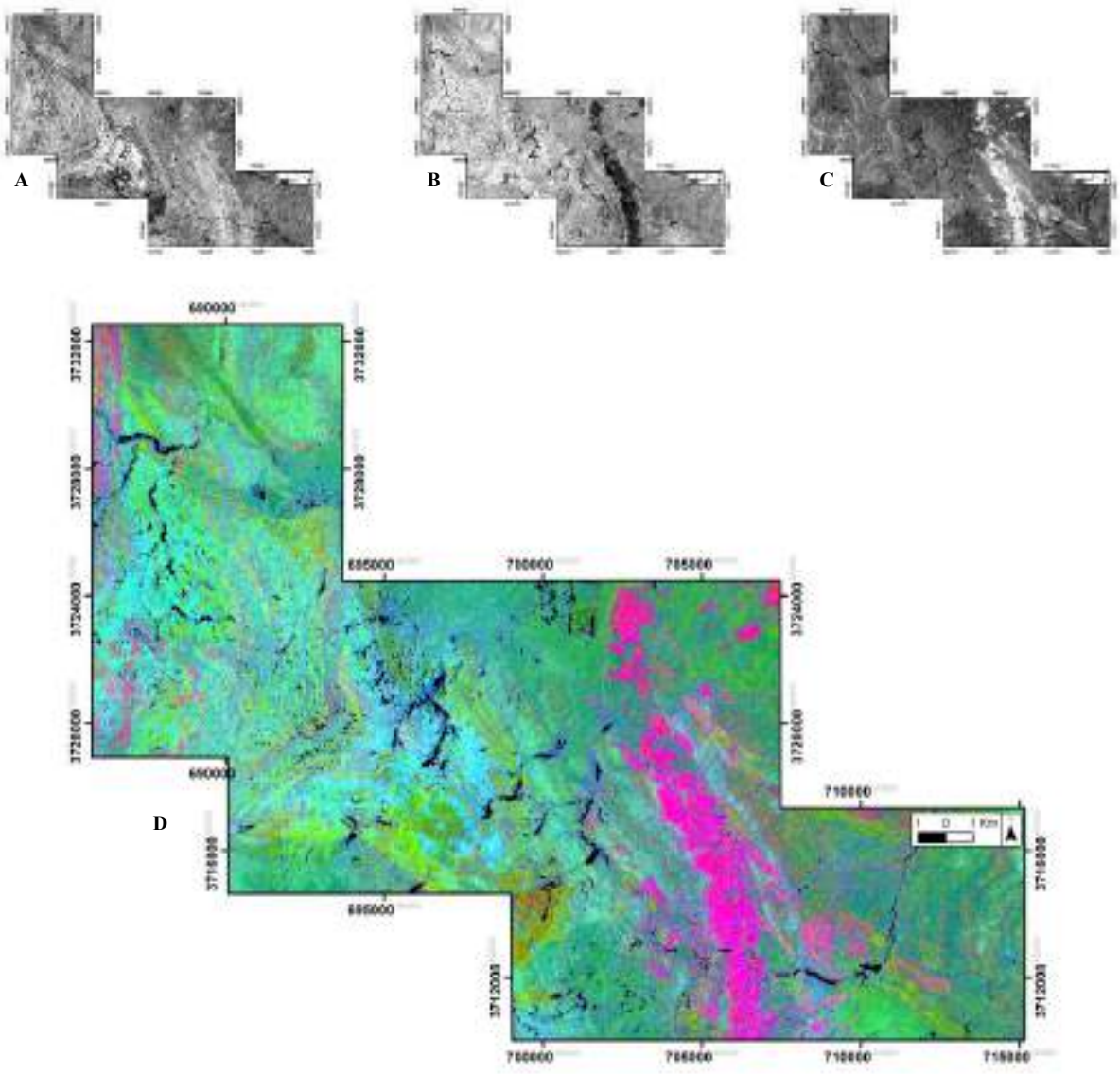

Fig 9 A) RBD5: Argillic Alteration, B) RBD6: Phyllic alteration, C) RBD8: Propylitic alteration, D) False-color composite image (R=RBD8, G=RBD6, B=RBD5).

3. Matched Filtering Result

In the MF method, after applying atmospheric corrections to each frame's raw image and resampling each indicator mineral's spectral curves, a picture is obtained using an available algorithm where the target points appear in white. The resulting image serves as a criterion in determining the threshold level, allowing the targets of interest to be highlighted. One advantage of thresholding is that inputting a specific alteration type's spectral signature can separate similar areas from the background (targets appear in white, and background areas appear in black). The resulting images are classified into several classes through unsupervised classification, creating a binary layer with a value of 1 for the desired areas. As these classified images may contain single-pixel regions, a Max-Min filter is applied according to the level and distribution of these single-pixel regions. The output is then transformed into a vector for integration and potential target area detection. Figs. 10 to 14 show the result of applying this method using the USGS spectral library for each mineral. Each image shows the SWIR spectrum of each mineral present in the area. The examined minerals include kaolinite, epidote, muscovite, and malachite.

Fig 10a corresponds to the identified areas for muscovite, predominantly covering the central part. As previously mentioned, muscovite indicates phyllic alteration and exhibits high absorption in the Aster band 6 (Fig 10b). Fig 11a depicts the scattering of kaolinite in the region, which is concentrated similarly to muscovite in the central part and has a high density. Fig 11b shows that this mineral also has high absorption in the Aster band 6. For epidote, the scattering is more pronounced in the eastern part of the area, following the trend of the Lakhha-ye-tangal and Asheghan mountains (Fig 12a), with high absorption in the Aster band 8 (Fig 12b). Malachite is predominantly found in the central part and around the Zul mountain (Fig 13).

Finally, all the highlighted spectra from each mineral are combined in Fig 14, indicating the co-occurrence of muscovite and kaolinite mineralization in the central region, with signs of malachite alongside them.

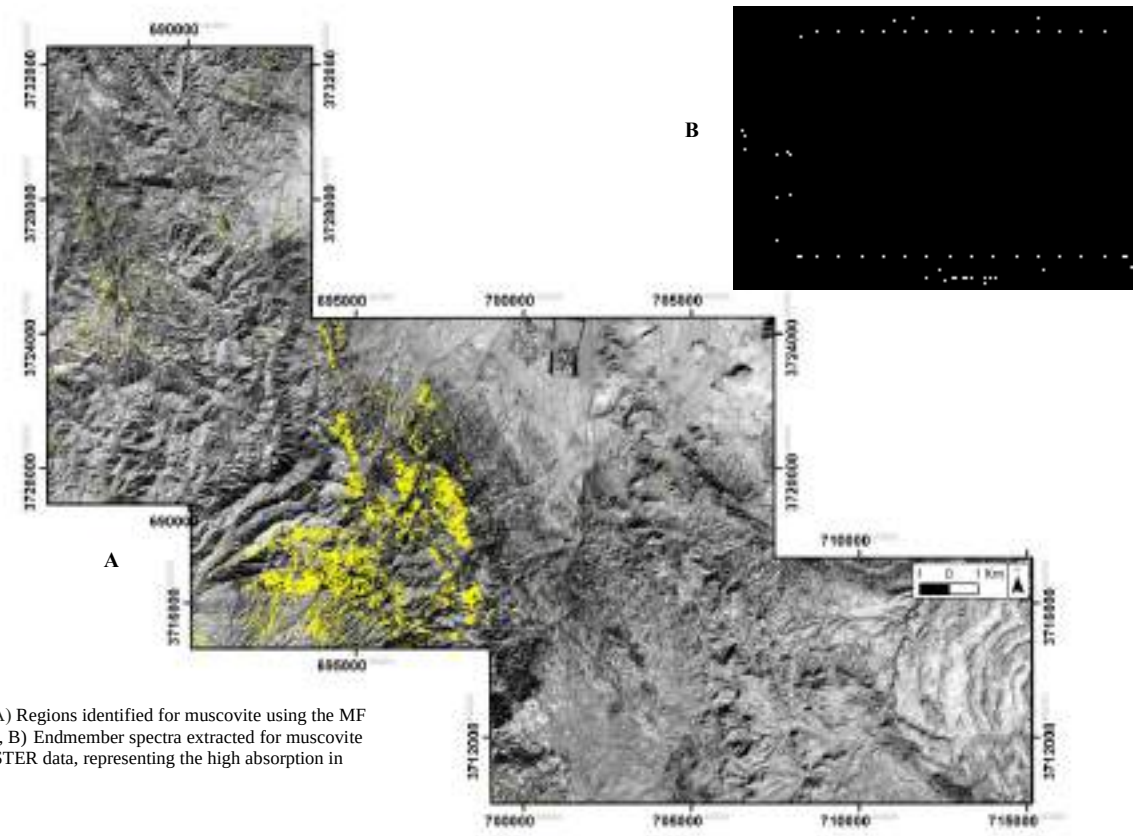

Fig 10 A) Regions identified for muscovite using the MF method., B) Endmember spectra extracted for muscovite from ASTER data, representing the high absorption in band 6.

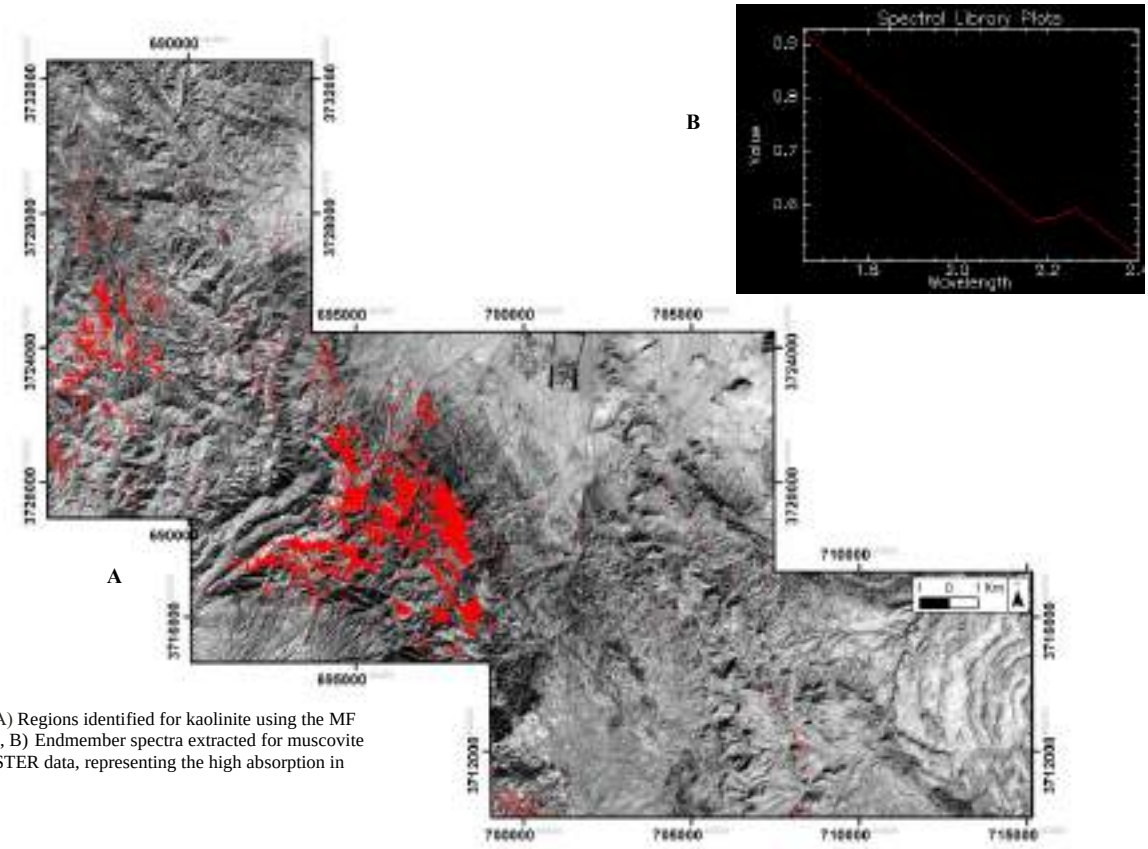

Fig 11 A) Regions identified for kaolinite using the MF method., B) Endmember spectra extracted for muscovite from ASTER data, representing the high absorption in band 6.

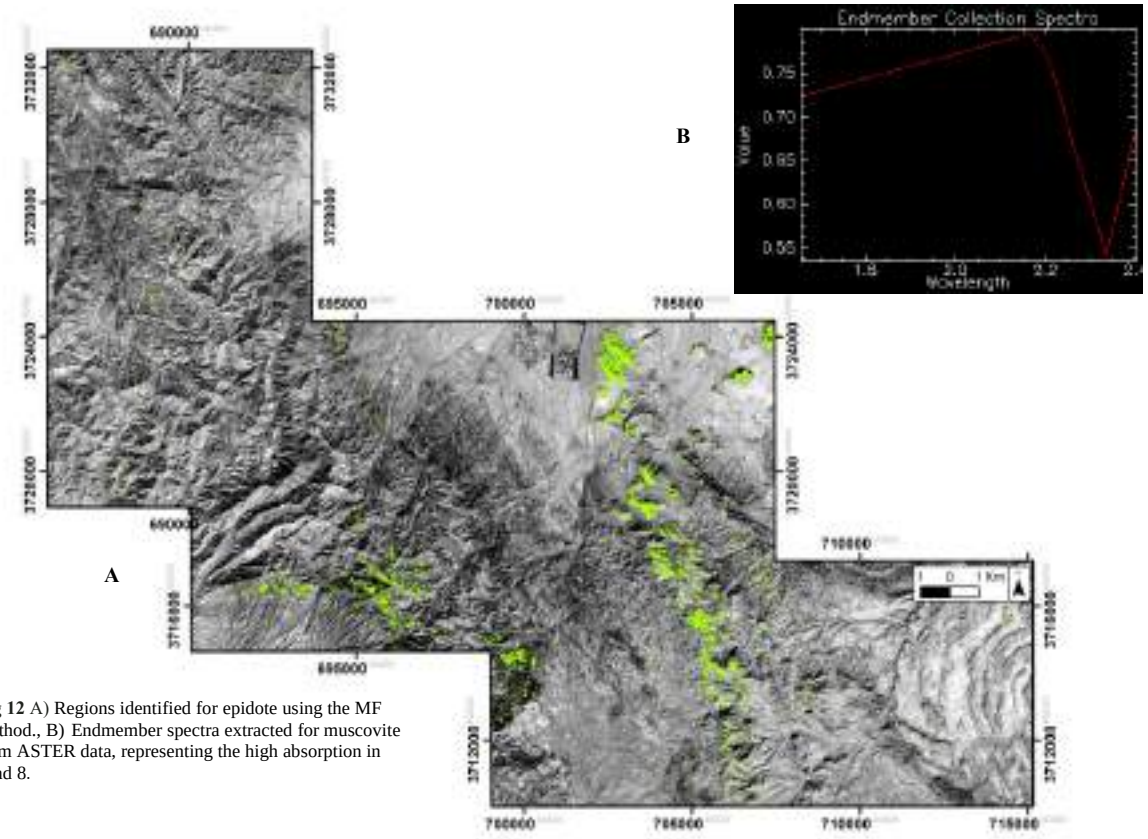

Fig 12 A) Regions identified for epidote using the MF method., B) Endmember spectra extracted for muscovite from ASTER data, representing the high absorption in band 8.

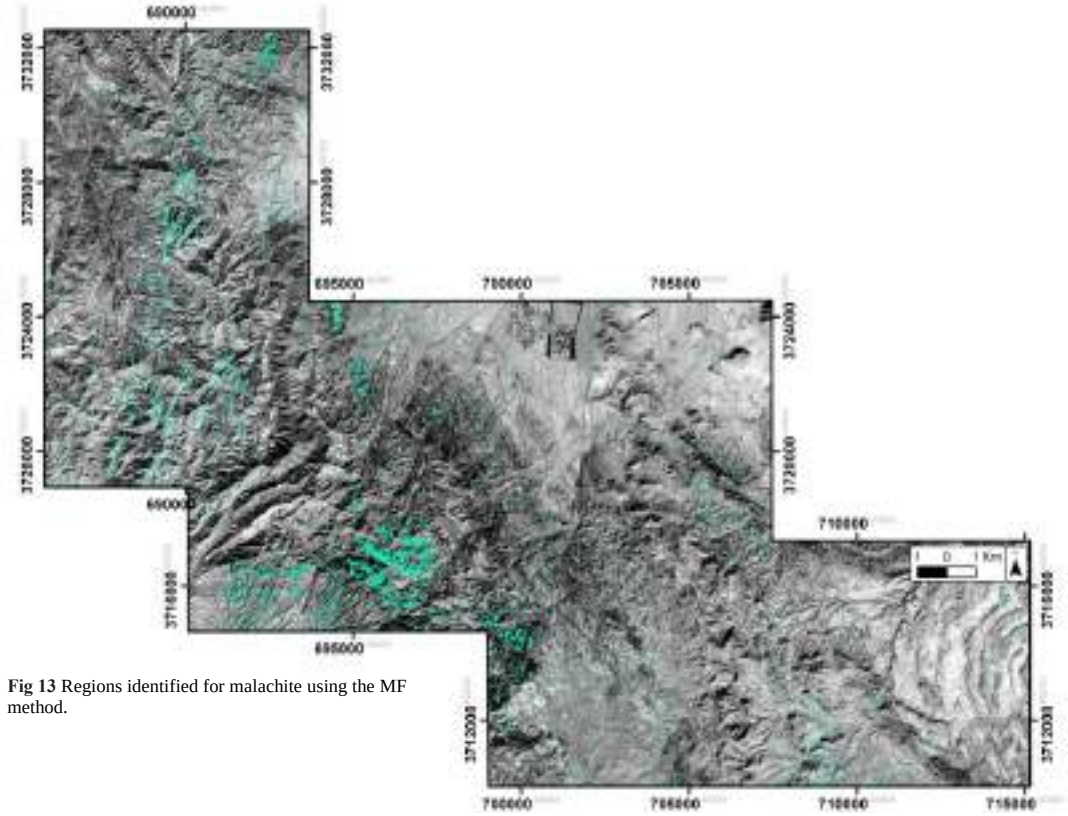

Fig 13 Regions identified for malachite using the MF method.

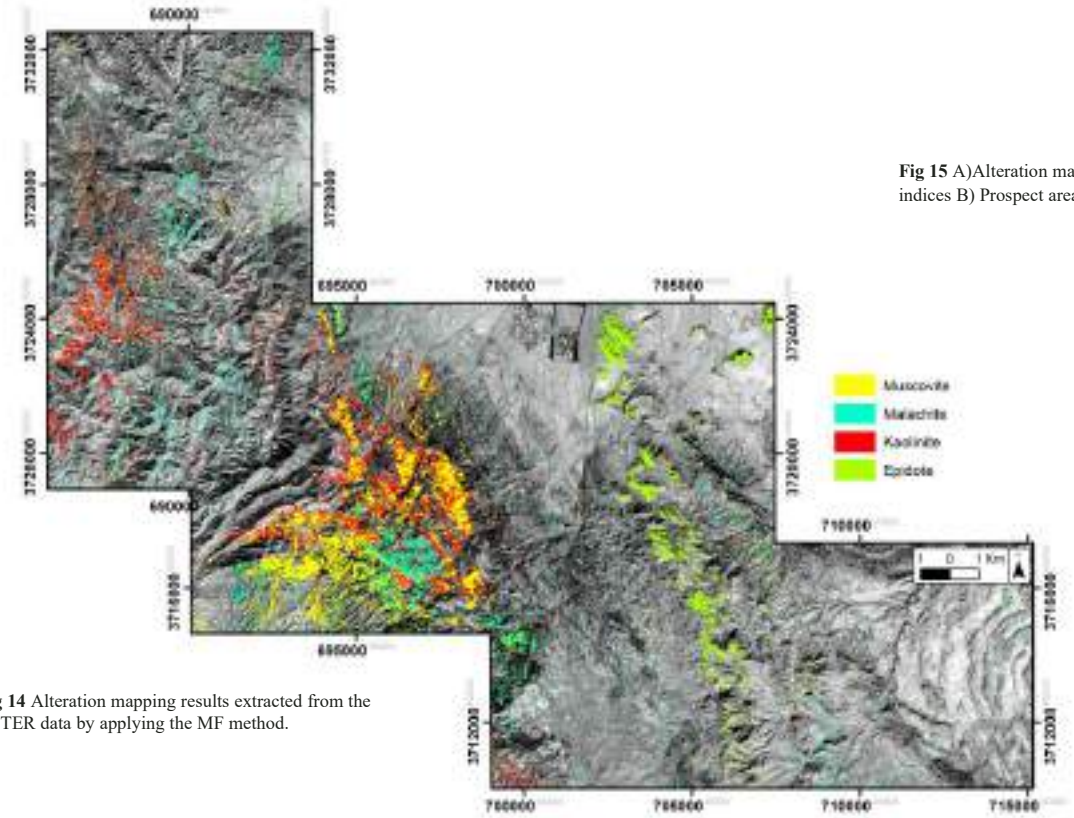

Fig 14 Alteration mapping results extracted from the ASTER data by applying the MF method.

Fig 15 A)Alteration mapping results with mineralized indices B) Prospect area for porphyry copper system

4. Discussion

ASTER images and analytical methods, including FCC (False Color Composite), BR (Band Ratio), RBD (Ratio-Band Depth), and MF (Matched Filtering), were employed for mapping hydrothermal minerals and related alterations. In the initial analysis, it can be noticed that almost all the utilized algorithms provide similar results. Still, regarding details and accuracy, the FCC method is relatively primary, offering a general overview of the area. On the other hand, the MF and BR methods exhibit the highest accuracy, emphasizing the target factors of this research in greater detail. It is worth noting that the region's low vegetation cover, further enhanced by the removal of vegetation using the NDVI method, significantly contributes to the precision of the analysis.

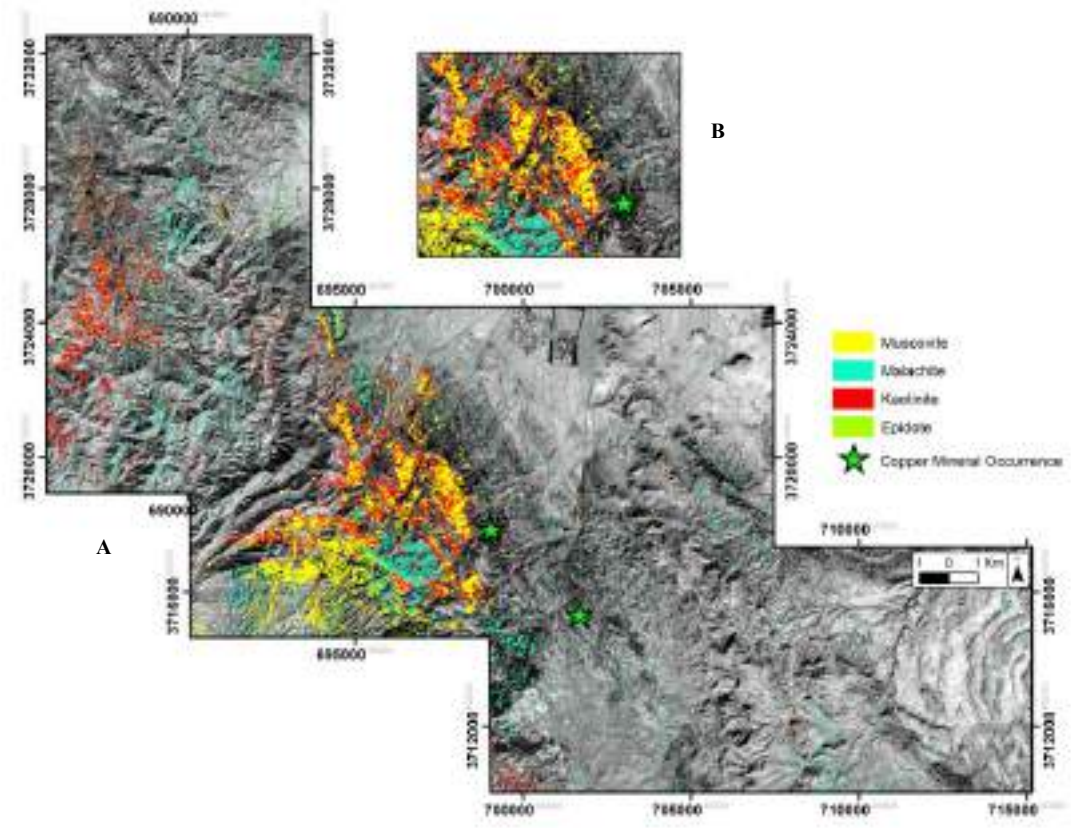

5. Conclusions

Concerning highlighting muscovite (phyllic alteration zone), the FCC method did not exhibit considerable accuracy. Nevertheless, it effectively demonstrated areas with epidote (propylitic alteration zone), outperforming the MF, BR, and RBD methods. The propylitic zone, situated on the Lakhhayetangal and Asheghan mountains in the eastern part of the region, has a lithology dating back to the Cretaceous period, forming an orbitoline-bearing limestone unit beneath Eocene Formations, constituting the Lakhdizuk Formation. In this unit, plagioclase has transformed into secondary minerals such as epidote and calcite due to alteration processes. In the argillic alteration zone, the combined results unequivocally indicate the presence of kaolinite and argillic alteration in the central area and around the Zul and Abidar mountains, especially on the Proterozoic units, which constitute the oldest lithological units in the region. The lithology of this unit is granite and occasionally migmatite, exhibiting a pink to brown color with a porphyritic texture.

The phyllic alteration, identified by the MF, BR, and RBD algorithms, is also present around and in contact with the argillic alteration and occurs on the gneissic and migmatite units, which are also of Proterozoic age. Regarding copper mineralization, it is worth mentioning that two mineralized indices (Fig 15a), Khunik-e-bala and Anjul, are located close to Zul Mountain. Copper mineralization in these areas occurs as epithermal and vein-type deposits associated with volcanic hosts. The locations identified by the MF for malachite are close to these two mineralized indices, indicating a high mineralization potential in the central part. Considering the geometric patterns of kaolinite and muscovite alterations, with the phyllic alteration surrounding and enclosing the phyllic alteration (Fig 15b), it is possible to infer a porphyry copper system in addition to the epithermal mineralization in this study area.

Data availability

Data will be made available on request.

References

Abrams, M., 2000. The advanced Spaceborne thermal emission and reflection radiometer (ASTER): Data products for the high spatial resolution imager on NASA's Terra platform. International Journal of Remote Sensing, 21, 847–859. https://doi.org/10.1080/014311600210326.

Abrams, M., Tsu, H., Hulley, G., Iwao, K., Pieri, D., Cudahy, T.J., Kargel, J., 2015. The advanced spaceborne thermal emission and reflection radiometer (ASTER) after fifteen years: a review of global products. Int. J. Appl. Earth Obs. Geoinf. 38, 292–301. http://dx.doi.org/10.1016/j.jag.2015.01.013.

Adiri, Z., El-Harti, A., Jellouli, A., Maacha, L., Bachaoui, E, M., 2016. Lithological mapping using Landsat 8 OLI and Terra ASTER multispectral data in the Bas Drâa inlier, Moroccan Anti Atlas. Journal of Applied Remote Sensing. 10. 016005. http://dx.doi.org/10.1117/1.JRS.10.016005.

Aghanabati, A., 1998. Jurassic stratigraphy of Iran, Geological Survey of Iran, Tehran, vol 1.

Aghanabati, A., 2004. Geology of Iran. Geological Survey of Iran.

Ahmadirouhani, R., Karimpour M,H,, Rahimi, B., Malekzadeh-Shafaroudi, A., Pour, AB., Pradhan, B., 2018. Integration of SPOT-5 and ASTER satellite data for structural tracing and hydrothermal alteration mineral mapping: implications for Cu-Au prospecting. Int J Image Data Fusion. 9(3):237–262. https://doi.org/10.1080/19479832.2018.1469548.

Alavi, M., 1991. Sedimentary and structural characteristics of the Paleo-Tethys remnants in northeastern Iran, Geological Society Of America., V.103., 150-160. https://doi.org/10.1130/0016-7606(1991)103%3C0983:SASCOT%3E2.3.CO;2.

Alimohammadi, M., Alirezaei, S., Kontak, D, J., 2015. Application of ASTER data for exploration of porphyry copper deposits: A case study of Daraloo–Sarmeshk area, southern part of the Kerman copper belt, Iran. Ore Geology Reviews, 70, 290–304. https://doi.org/10.1016/j.oregeorev.2015.04.010.

Alipour. M, Sa'adadin, N., et al., 2008. Geochemical Exploration in Qaen 1.100000 Sheet, Geological Survey of Iran.

Amer, R., Kusky, T., Ghulam, A., 2010. Lithological mapping in the Central Eastern Desert of Egypt using ASTER data. Journal of African Earth Sciences - J AFR EARTH SCI. 56. 75–82. http://dx.doi.org/10.1016/j.jafrearsci.2009.06.004.

Azizi, H., Tarverdi, M, A., Akbarpour, A., 2010. Extraction of hydrothermal alterations from ASTER SWIR data from east Zanjan, northern Iran. Advances in Space Research, 46(1), pp.99-109. http://dx.doi.org/10.1016/j.asr.2010.03.014.

Bedini, E., 2011. Mineral mapping in the Kap Simpson complex, central East Greenland, using HyMap and ASTER remote sensing data. Advances in Space Research, 47(1), pp.60–73. http://dx.doi.org/10.1016/j.asr.2010.08.021.

Berberian. M., and King, G.C.P., 1981, Towards a paleogeography and tectonic evolution of Iran: Canadia n Journal of Earth Sciences, v. 18, no. 2, p. 210–265. http://dx.doi.org/10.1139/e81-019.

Berthiaux. A., Christmann. P., Fauvelet, E., Hatrival, J,N., Maurizot, P., Vaslet, D., 1979. Geology paper 1:100.000 Qaen. Geological Survey of Iran, Sheet No. 7857.

Berthiaux. A., Christmann. P., Fauvelet, E., Hatrival, J,N., Maurizot, P., Vaslet, D., 1999. Geology paper 1:250.000 Qaen. Geological Survey of Iran, Sheet No. K7.

Ben-Dor, E., Kruse, F, A., 1994. The relationship between the size of spatial subsets of GER 63 channel scanner data and the quality of the Internal Average Relative Reflectance (IARR) atmospheric correction technique. Remote Sensing, 15(3), pp.683-690. https://doi.org/10.1080/01431169408954107.

Boloki, M., Poormirzaee, M., 2010. Using ASTER image processing for hydrothermal alteration and key alteration minerals mapping. Journal of Latest Trends on Engineering Mechanics, Structures, Engineering Geology, 1, pp.77-82.

Boardman, J, W., Kruse, F, A., Green, R, O., 1995. Mapping target signatures via partial unmixing of AVIRIS data. Proceedings of the Fifth JPL Airborne Earth Science Workshop, Pasadena, California 95–01, p. 2326.

Camp, V, E., Griffis, R, J., 1982. character, genesis, and tectonic setting of igneous rocks in the Sistan suture zone. Lithos, 15, pp. 21 – 239. http://dx.doi.org/10.1016/0024-4937(82)90014-7.

Clark, R, N., Swayze, G, A., Gallagher, A., King, T., Calvin, W.M., 1993. The U.S. Geological Survey, Digital Spectral Library: Version 1: 0.2 to 3.0 microns: U.S. Geological Survey Open-File Report 93-592, 1340 p.

Crowley, J, K., Brickey, D, W., Rowan, L, C., 1989. Airborne imaging spectrometer data of the Ruby Mountains, Montana: mineral discrimination using relative absorption band-depth images. Remote Sensing of Environment, 29(2), pp.121–134. https://doi.org/10.1016/0034-4257(89)90021-7.

Crosta, A,P., De Souza Filho, C,R., Azevedo, F., Brodie, C., 2003. Targeting key alteration minerals in epithermal deposits in Patagonia, Argentina, using ASTER imagery and principal component analysis. Int. J. Remote Sens. 24, 4233–4240. https://doi.org/10.1080/0143116031000152291.

Fujisada, H., 1995. Design and performance of ASTER instrument. In: J.B. Breckinridge (Ed.), Proceedings of International Society of Optical Engineering, 2583, pp. 16–25. Paris, France: SPIE. https://doi.org/10.1117/12.228565.

Ghorbani, M., 2013. The Economic Geology of Iran: Mineral Deposits and Natural Resources. Springer, Dordrecht, 1–450. https://doi.org/10.1007/978-94-007-5625-0.

Ghorbani, M., Tajbakhsh, P., Khoi, N., 2000. Lead-zinc deposits in Iran. Geological Survey of Iran, 512 p.

Harsanyi, J, C., Farrand, W., Chang, C, I., 1994. April. Detection of subpixel spectral signatures in hyperspectral image sequences. In Annual Meeting, Proceedings of American Society of Photogrammetry & Remote Sensing (pp. 236-247).

Hewson, R., Cudahy, T., 2011. Issues affecting geological mapping with ASTER data: a case study of the Mt Fitton area, South Australia, in Land Remote Sensing and Global Environmental CHANGE, NASA's Earth Observing System and the Science of ASTER and MODIS, B. Ramachandran, C. Justice, and M. J. Abrams, Eds., pp. 273–300. http://dx.doi.org/10.1007/978-1-4419-6749-7_13.

Hewson, R., Cudahy, T., Mizuhiko, S., Ueda, K., Mauger, A., 2005. Seamless geological map generation using ASTER in the

Broken Hill-Curnamona province of Australia. Remote Sensing of Environment - REMOTE SENS ENVIRON. 99. 159-172. http://dx.doi.org/10.1016/j.rse.2005.04.025.
Hunt, G,R., Ashley, R,P., 1979. Spectra of altered rocks in the visible and near-infrared: Econ. Geol., 74(7): 1613–1629. https://doi.org/10.2113/gsecongeo.74.7.1613.
Hunt, G,R., 1977. Spectral signatures of particulate minerals in the visible and near-infrared. Geophysics, 42(3): 501–513. https://doi.org/10.1190/1.1440721.
Iwasaki, A., Fujisada, H., Akao, H., Shindou, O., Akagi, S., 2002. Enhancement of spectral separation performance for ASTER/SWIR. Proceedings of SPIE. Infrared Spaceborne Remote Sensing IX. 4486. http://dx.doi.org/10.1117/12.455140.
Jun, L., Songwei, C., Duanyou, L., Bin, W., Shuo, L. Liming, Z., 2008. Research on false color image composite and enhancement methods based on ratio images, the international archives of the photogrammetry. Remote Sensing and Spatial Information Sciences, Vol. 37, pp. 1151-1154.
Kruse, F, A., 1988. Use of Airborne Imaging Spectrometer data to map minerals associated with hydrothermally altered - rocks in the northern Grapevine Mountains, Nevada and California, Remote Sensing of Environment, V. 24, No. 1, p. 31-51.
Liang, S., Li, X., Wang, J., 2012. Advanced Remote Sensing, Chapter 5, Academic Press is an imprint of Elsevier, p.122 -124.
Liu, L., Li, Y., Zhou, J., Han, L., Xu, X., 2018. Gold-copper deposits in Wushitala, Southern Tianshan, Northwest China: Application of ASTER data for mineral exploration. Geological Journal. 53(S2): 362–371. https://doi.org/10.1002/gj.2989.
Maghsoudi, A., Rahmani, M., Rashidi, B., 2005. Gold deposits and indications of Iran. Research manual for Students of Earth Science (In Persian).
Marzouki, A., Dridri, A., 2023. Lithological discrimination and structural lineaments extraction using Landsat 8 and ASTER data: a case study of Tiwit (Anti-Atlas, Morocco). Environ Earth Sci 82, 125. https://doi.org/10.1007/s12665-023-10831-4.
Mars, J, C., 2014. Regional mapping of hydrothermally altered igneous rocks along the Urumieh-Dokhtar, Chagai, and Alborz Belts of western Asia using Advanced Spaceborne Thermal Emission and Reflection Radiometer (ASTER) data and Interactive Data Language (IDL) logical operators: a tool for porphyry copper exploration and assessment. Scientific Investigations Report 2010-5090-O. https://doi.org/10.3133/sir20105090O.
Mars, J, C., Rowan, L, C., 2006. Regional mapping of phyllic and argillic altered rocks in the Zagros magmatic, Iran, using Advanced Spaceborne Thermal Emission and Reflection Radiometer (ASTER) data and logical operator algorithms. Geosphere, v.2, No.3, p. 161–186, https://doi.org/10.1130/GES00044.1.
Matthew, M,W., AdlerGolden, S., Berk, A., Felde, G., Anderson, G,P., Gorodetzky, D., Paswaters, S., Shippert, M., 2002. Atmospheric correction of spectral imagery: Evaluation of the FLAASH algorithm with AVIRIS data. Proceedings of SPIE - The International Society for Optical Engineering. 5093. 157 - 163. http://dx.doi.org/10.1109/AIPR.2002.1182270.
Modabberi, S., Ahmadi, A., Tangestani, M, H., 2017. Sub-pixel mapping of alunite and jarosite using ASTER data; a case study from north of Semnan, north central Iran, Ore Geology Reviews 80,429 -436. http://dx.doi.org/10.1016/j.oregeorev.2016.07.014.
Moghtaderi, A., Moore, F., Mohammadzadeh, A., 2007. The application of advanced apace-borne thermal emission and reflection (ASTER) radiometer data in the detection of alteration in the Chadormalu Paleocrater, Bafq region, Central Iran. Journal of Asian Earth Sciences, 30, 238–252. https://doi.org/10.1016/j.jseaes.2006.09.004.
Moghtaderi, A., Moore, F., Ranjbar, H., 2017. Application of ASTER and Landsat 8 imagery data and mathematical evaluation method in detecting iron minerals contamination in the Chadormalu iron mine area, central Iran. Journal of Applied Remote Sensing, 11, 1-16. https://doi.org/10.1117/1.JRS.11.016027.
Moradpour, H., Rostami Paydar, G., Feizizadeh, B., Blaschke, T., 2021. Landsat-7 and ASTER remote sensing satellite imagery for identification of iron skarn mineralization in metamorphic regions. International Journal of Image and Data Fusion, 13, 71-94. https://doi.org/10.1080/10106049.2020.1810327.
QUAC., 2009. Atmospheric Correction Module: QUAC and FLAASH User's Guide.
Rowan, L, C., Goetz, A, F, h., Ashley, R, P., 1977. Discrimination of hydrothermally altered rocks and unaltered rocks in visible and Near-infrared multispectral images: Geophysics, v. 42, p. 522-535. https://doi.org/10.1190/1.1440723.
Rowan, L, C., Mars, J, C., 2003. Lithologic mapping in the Mountain Pass, California area using Advanced Spaceborne Thermal Emission and Reflection Radiometer (ASTER) data. Remote Sensing of Environment, 84, 350–366. https://doi.org/10.1016/S0034-4257(02)00127-X.
Rowan, L, C., Mars, J, C., & Simpson, C. J., 2005. Lithologic mapping of the Mordor, NT, Australia ultramafic complex by using the Advanced Spaceborne Thermal Emission and Reflection Radiometer (ASTER). Remote Sensing Environment, 99, 105–126. https://doi.org/10.1016/j.rse.2004.11.021.
Rani, N., Mandla, V, R., Singh, T.,2017. Evaluation of atmospheric corrections on hyperspectral data with special reference to mineral mapping. Geosci. Front. 8, 797–808. http://dx.doi.org/10.1016/j.gsf.2016.06.004.
Shahmoradi, A., Yazdi, M., 2023. Enhancement of susceptible iron regions in the Kamo area by correlation of geological, magnetometry, and remote sensing data. 15th Symposium of Iranian Society of Economic Geology (In Persian).
Stöcklin, J., Eftekharnezhad, J., Hushmandzadeh, A., 1972. Central Lut reconnaissance, East Iran. Geological Survey Iran, report no. 22, 62 p.
Tahir, T., Caner, D,. 2022. Remote sensing of Listvenite rock for Kaymaz Gold Deposit, Eskişehir-TÜRKİYE. Journal of Geochemical Exploration. 243. 107110. http://dx.doi.org/10.1016/j.gexplo.2022.107110.
Tangestani, M, H., Mazhari, N., Ager, B., & Moore, F., 2008. Evaluating advanced spaceborne thermal emission and reflection radiometer (ASTER) data for alteration zone enhancement in a semi-arid area, northern Shahr-e-Babak, SE Iran. Int. J. Rem. Sens., 29(10): 2833-2850. http://dx.doi.org/10.1080/01431160701422239.
Testa, F, J., Villanueva, C., Cooke, D,R., Zhang, L., 2018. Lithological and Hydrothermal Alteration Mapping of Epithermal, Porphyry and Tourmaline Breccia Districts in the Argentine Andes Using ASTER Imagery. Remote Sensing. 2018, 10, 203, http://dx.doi.org/10.3390/rs10020203.
Tirrul, R., Bell, I.R., Griffis, R.J., Camp, V.E., 1983.The Sistan Suture Zone of Eastern Iran, Geological Society of American Bulletin, V 94, 134-150.http://dx.doi.org/10.1130/0016-7606(1983)94%3C134:TSSZOE%3E2.0.CO;2
Zhang, X., Pazner, M., Duke, N., 2007. Lithologic and mineral information extraction for gold exploration using ASTER data in the south Chocolate Mountains (California). ISPRS Journal of Photogrammetry and Remote Sensing. 62. 271-282. http://dx.doi.org/10.1016/j.isprsjprs.2007.04.004.